Hindawi
Advances in Polymer Technology
Volume 2020, Article ID 7819049, 12 pages
https://doi.org/10.1155/2020/7819049

Research Article

A Nitrogen-Rich Covalent Triazine Framework as a Photocatalyst for Hydrogen Production

Ruizhi Gong,[1] Liuliu Yang,[1] Shuo Qiu,[1] Wan-Ting Chen,[2] Qing Wang,[2] Jiazhuo Xie,[3] Geoffrey I. N. Waterhouse,[1,2,4] and Jing Xu[1]

[1]*College of Chemistry and Material Science, Shandong Agricultural University, Tai'an, Shandong 271018, China*
[2]*School of Chemical Sciences, The University of Auckland, Auckland, New Zealand*
[3]*College of Resources and Environment, Shandong Agricultural University, Tai'an, Shandong 271018, China*
[4]*The MacDiarmid Institute for Advanced Materials and Nanotechnology, New Zealand*

Correspondence should be addressed to Geoffrey I. N. Waterhouse; g.waterhouse@auckland.ac.nz and Jing Xu; jiaxu@sdau.edu.cn

Received 18 February 2020; Accepted 15 April 2020; Published 7 May 2020

Academic Editor: Yuezhong Meng

Covalent triazine frameworks (CTFs) have emerged as new candidate materials in various research areas such as catalysis, gas separation storage, and energy-related organic devices due to their easy functionalization, high thermal and chemical stability, and permanent porosity. Herein, we report the successful synthesis of a CTF rich in cyano groups (CTF-CN) by the solvothermal condensation of 2,3,6,7-tetrabromonapthalene (TBNDA), Na_2(1,1-dicyanoethene-2,2-dithiolate), and 1,3,5-tris-(4-aminophenyl)-triazine (TAPT) at 120°C. XRD, SEM, and TEM characterization studies revealed CTF-CN to be amorphous and composed of ultrathin 2D sheets. CTF-CN possessed strong absorption at visible wavelengths, with UV-vis measurements suggesting a band gap energy in the range 2.7-2.9 eV. A 5 wt.% Pt/CTF-CN was found to be a promising photocatalyst for hydrogen production, affording a rate of 487.6 μmol g^{-1} h^{-1} in a H_2O/TEOA/CH_3OH solution under visible light. The photocatalytic activity of CTF-CN was benchmarked against g-C_3N_4 for meaningful assessment of performance. Importantly, the 5 wt.% Pt/CTF-CN photocatalyst exhibited excellent thermal and photocatalytic stability. Further, as a nitrogen-rich porous 2D material, CTF-CN represents a potential platform for the development of novel electrode material for fuel cells and metal ion batteries.

1. Introduction

Energy production and storage are two of the biggest challenges for the 21st century. There is increasing global demand for environmentally friendly energy sources, with the solar-driven splitting of water into H_2 and O_2 receiving a lot of attention as a potentially sustainable source of H_2 fuel. Over the past decade, interest in the development of visible light-driven photocatalysts for hydrogen production has grown enormously [1–3]. Graphitic carbon nitride (g-C_3N_4), a 2D polymeric material based on heptazine units, has emerged as the front runner in this field owing to its ease of synthesis from a variety of nitrogen-rich organic molecules, its tuneable band gap (E_g = 2.2-2.8 eV) which can be adjusted by varying the nitrogen level or heteroatom doping, and the favourable locations of its valence and conduction band levels (+1.57 eV and -1.12 eV, respectively) [4–6]. The position of the valence band maximum allows water oxidation (O_2/H_2O = 0.82 V at pH 7), whilst the position of the conduction band minimum allows proton reduction to H_2 (H_2O/H_2 = −0.41 V at pH 7) [7, 8]. H_2 production rates can be greatly enhanced by the addition of a metal cocatalyst (typically Pt) and a sacrificial hole scavenger (typically methanol or triethanolamine) [9, 10]. A further feature of g-C_3N_4, which distinguishes it from many other visible light-driven photocatalysts, is its excellent stability [11, 12]. Appreciation of the many favourable attributes of g-C_3N_4 has prompted researchers to synthesize molecular analogues, in particular covalent triazine frameworks (CTFs) which are a special subcategory of covalent organic frameworks (COFs) [13]. CTFs exhibit many of the same physical and optical properties as g-C_3N_4, making them particularly attractive synthetic

targets as "molecular" heterogeneous photocatalysts for H_2 production.

Cote and coworkers first demonstrated the utility of topological design principles in connecting molecular building blocks via covalent bonds, thereby creating COFs with large specific surface areas and low density [14]. COFs are now widely applied in gas adsorption, gas storage, fuel cell technology, sensing, heterogeneous catalysis, and photocatalytic applications [15]. Kuhn et al. subsequently pioneered the development of CTFs [13], COFs based primarily on C, H, and N with high thermal stabilities and permanent porosity. CTFs are superior to many traditional porous materials (such as zeolites) in hydrogen storage, gas adsorption, gas separation, and heterogeneous catalysis [16–18]. Triazine rings have similar aromaticity as benzene rings and high electron affinities, along with excellent thermal and chemical stabilities making them especially suitable for catalyst and photocatalyst construction, whilst the presence of nitrogen in triazine results in a modest HOMO-LUMO separation allowing for visible light excitation. Kamiya and coworkers reported that a platinum-modified CTF hybridized with conductive carbon nanoparticles showed excellent activity and selectivity for oxygen reduction reactions in the presence of methanol [19]. Ding et al. reported that a palladium-modified imine-linked COF showed good catalytic activity, stability, and recyclability for Suzuki-Miyaura coupling reactions [20]. Bi et al. examined the photocatalytic performance of a CTF with a graphene-like layered morphology for H_2 production. In the presence of a platinum cocatalyst, a H_2 production rate of ~250 μmol g^{-1} h^{-1} was realized in 12.5 vol% TEOA under $\lambda > 420$ nm excitation. Huang et al. successfully synthesized covalent triazine frameworks with benzothiadiazoles and thiophene moieties as electron-withdrawing and electron-donating units, respectively. A remarkable H_2 evolution rate of 6.6 mmol g^{-1} h^{-1} was achieved under visible light irradiation ($\lambda > 420$ nm) for one of the CTF hybrids synthesized, with the high activity being rationalized in terms of the improved charge separation that was possible in such hybrid CTF systems. These studies highlight the enormous untapped potential of CTFs as visible light-driven photocatalysts for H_2 production [21]. However, most of the studies reported in the literature relating to CTF development for photocatalytic H_2 production do not include data for an appropriate reference photocatalyst under the same testing conditions [22–24]. This makes it is very difficult to meaningfully compare the activity of CTFs prepared by different research groups in terms of their H_2 production performance [25–27]. More comparative studies are needed, where new CTFs are tested alongside a reliable catalyst standard, such as g-C_3N_4.

A number of studies have shown that the introduction of cyano groups (-C≡N) into g-C_3N_4 photocatalysts can be beneficial for improving the visible light response and photocatalytic activity [28–30]. Cyano groups have strong electron-withdrawing properties and thus promote the efficient separation of photogenerated electrons and holes. Cyano groups also offer a functional group that can easily be modified chemically to impart additional functionality into a molecule or a polymer. To date, the synthesis of CTFs containing an abundance of cyano groups has received little attention, thus motivating a detailed investigation.

In this work, we aimed to synthesize a novel cyano-containing CTF (denoted herein as CTF-CN) via a facile solvothermal synthesis method. Our approach involved the reaction of 2,3,6,7-tetrabromonapthalene dianhydride (TBNDA) with Na_2(1,1-dicyanoethene-2,2-dithiolate), followed by the condensation reaction of the organic product of this reaction with 2,4,6-tris(4-aminophenyl)-1,3,5-triazine (TAPT) [31–33]. The reaction scheme and structure of the CTF-CN product is shown in Figure 1. The introduction of the conjugated naphthalene dianhydride units was expected to assist visible light absorption; the TAPT component would impart stability, whilst the dicyano groups would offer sites for postsynthetic modification of the covalent framework. By synergistically combining these attributes, it was anticipated that a CTF material with good photocatalytic activity for visible light-driven hydrogen production could be synthesized [34, 35].

2. Experimental Section

2.1. Materials. 4-Aminobenzonitrile, trifluoromethanesulfonic acid, 2,3,6,7-tetrabromonapthalene, 1,3,5-tris-(4-aminophenyl)-triazine, carbon disulfide, N,N-dimethylformamide, n-butanol, mesitylene, triethanolamine, and all other chemicals were purchased from Aladdin and used without further purification. For the photocatalytic tests, Milli-Q water (18.2 MΩ·cm) was used.

2.2. Synthesis of 1,3,5-Tris-(4-aminophenyl) Triazine (TAPT). TAPT was synthesized via superacid catalyzed trimerization of 4-aminobenzonitrile. Briefly, 4-aminobenzonitrile (0.386 g) was added to a 25 mL three-neck round bottom flask equipped with a magnetic stirrer and N_2 inlet. Next, the flask was cooled to 0°C in an ice bath, after which 1 mL of trifluoromethanesulfonic acid (11.1 mmol) was added dropwise into the flask over a period of 1 h under magnetic stirring. The solution was then stirred for further 24 h at room temperature resulting in the formation of an orange precipitate. After completion of the reaction, distilled water (10 mL) was added to the mixture under constant stirring, and the mixture neutralized to pH 7 by the addition of 2 mol L^{-1} NaOH solution. As the pH increased, the orange precipitate dissolved to give a bright orange solution, with a pale yellow precipitate forming as the pH approached 7. The resultant pale yellow product was collected by filtration and then washed repeatedly with distilled water. The crude product was dried at 80°C under vacuum for 12 h, then purified by recrystallization in N-methylpyrrolidone (NMP). The recrystallized yellow TAPT product was dried overnight at 100°C. The purity of the TAPT product (yield 78.6%) was confirmed by elemental analysis and ^{1}H NMR spectroscopy.

2.3. Synthesis of Na_2(1,1-dicyanoethene-2,2-dithiolate) (Na_2(i-mnt)). Malononitrile (66 g, 1 mol) was slowly added to a stirred solution of sodium hydroxide (80 g) in ethanol (900 mL), with the temperature of the solution being maintained at 10°C. Next, carbon disulfide (76 g, 1 mol) was added dropwise over a period of 30 min, with the resulting pale

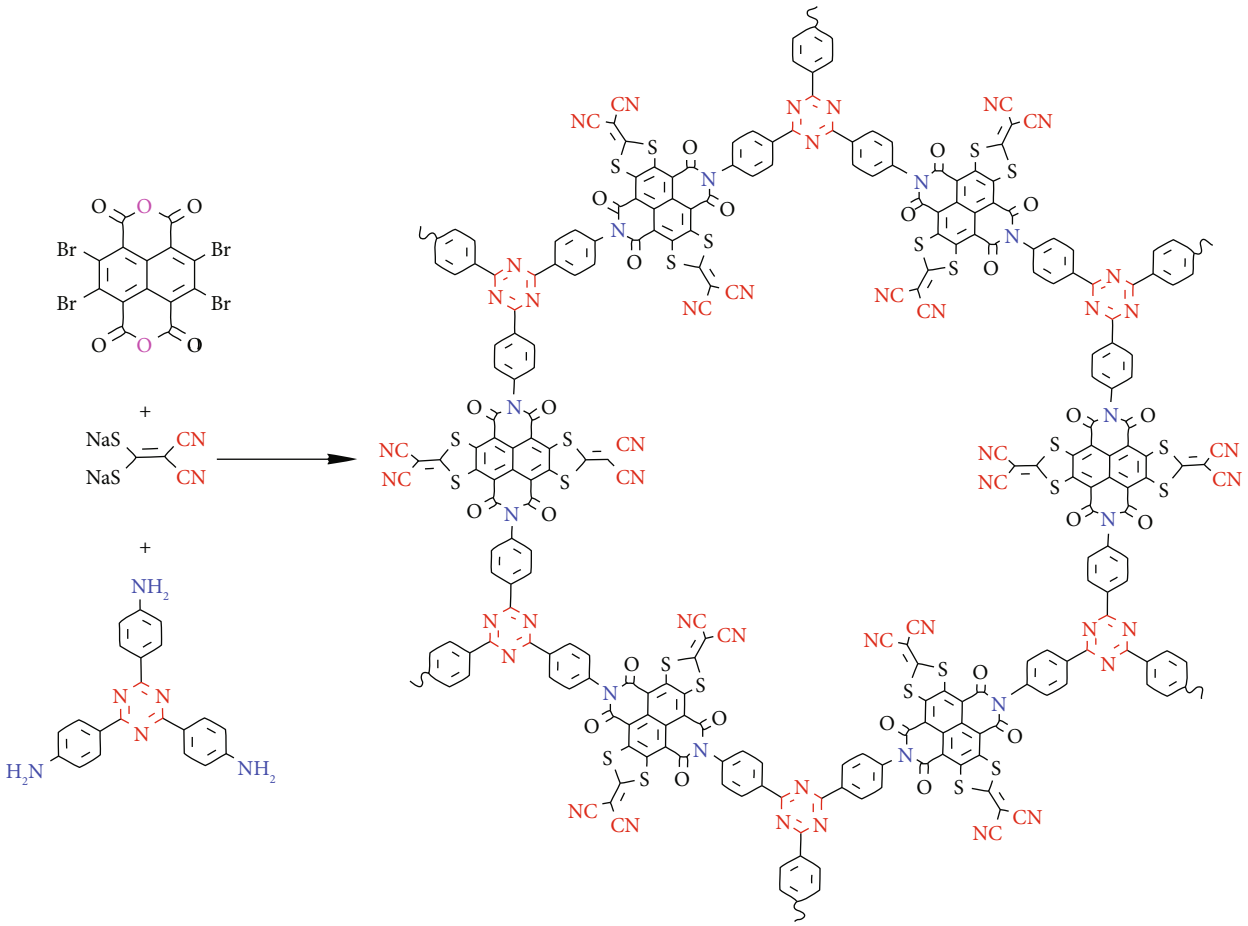

Figure 1: Scheme outlining the synthesis of CTF-CN.

yellow slurry then stirred for 1 h at room temperature. The product was collected by filtration, washed repeatedly with ethanol, and then dried at 80°C in a vacuum oven for 24 h. After drying, the product has a light brown colour and was mildly hydroscopic.

2.4. Synthesis of the Covalent Triazine Framework with Cyano Groups (CTF-CN). A 10 mL pyrex tube with a screw cap was charged with 2,3,6,7-tetrabromonapthalene (70 mg, 0.12 mmol) and Na_2(i-mnt) (44.8 mg, 0.241 mmol). To that mixture, n-butanol (3.91 mL) and mesitylene (1.31 mL) were added. The resulting mixture was then sonicated for 10 min to homogeneously disperse all the reactants. Next, the mixture was heated in an oil bath at 50°C for 1 h, after which 1,3,5-tris-(4-aminophenyl)-triazine (28 mg, 0.079 mmol) was added. The pyrex tube was then capped, and the reaction mixture was heated at 120°C for five days. The molar ratios of TBNDA, Na_2(i-mnt), and TAPT used in the synthesis were 1.5 : 3 : 1. The obtained black product was collected by filtration and washed with THF and acetone three times. The product (CTF-CN) was purified in a Soxhlet apparatus with MeOH and then dried under vacuum at 120°C for 12 h. The yield was ~90%.

2.5. Synthesis of the Graphitic Carbon Nitride (g-C_3N_4) Reference Photocatalyst. A g-C_3N_4 reference photocatalyst was prepared by the thermal polymerization of urea. Briefly, urea (30 g) was loaded into a 100 mL alumina crucible, covered with a lid, and then heated in a muffle furnace from room temperature to 550°C in air at a heating rate of 2°C min^{-1}. The crucible was held at 550°C for 4 h, then kept in the furnace and allowed to cool naturally to room temperature overnight. A yellow product was obtained.

2.6. Characterization. Elemental analyses on TAPT, TBNDA, Na_2(i-mnt), CTF-CN, and g-C_3N_4 were performed at the Campbell Microanalytical Lab (University of Otago, New Zealand). Attenuated total reflectance infrared (ATR-IR) spectra were recorded on an ALPHA FT-IR spectrometer over the 400-4000 cm^{-1} range. 32 scans at 4 cm^{-1} resolution were coadded to produce a spectrum. Powder X-ray diffraction (PXRD) patterns were collected on a Bruker AXS D-8 Advanced SWAX diffractometer equipped with a Cu-Kα source (0.15406 nm, 40 kV, 300 mA). The scan rate was of 0.02° s^{-1}. ^{1}H nuclear magnetic resonance (NMR) spectra were recorded on a 400 MHz spectrometer (Bruker Ascend 400 MHz NMR spectrometer). Samples were dissolved in deuterated DMSO for the analyses. Thermogravimetric analyses (TGA) were performed on a Linser T6/DTA thermoanalyzer instrument. Samples were heated at 10°C min^{-1} under a nitrogen gas flow. Scanning electron microscopy (SEM) images were recorded on a high-resolution scanning electron

microscope (Philips XL-30S Field Emission Gun scanning electron microscope). High-resolution transmission electron microscopy (HR-TEM) images were collected on a JEOL JEM 2010 transmission electron microscope operated at an electron accelerating voltage 200 kV. Samples were dispersed in absolute ethanol; then, 1 μL of the resulting dispersion transferred onto a holey carbon-coated copper TEM grid for analysis. UV-visible diffuse reflectance spectra were recorded on a UV 2410PC spectrometer equipped with an integrating sphere attachment. Fluorescence spectra were recorded on a RF-5301 PC spectrofluorophotometer (Shimadzu) with 1.0 cm path length cell. X-ray photoelectron spectroscopy (XPS) data were collected on a Thermo ESCALAB 250 equipped with an Al Kα X-ray source (hν = 1486.7 eV). N_2 physisorption data was collected at 77 K on a Tristar 2020 instrument. Specific surface areas were calculated from N_2 adsorption data in the p/p_0 range 0.01-0.1 by the Brunauer-Emmett-Teller (BET) method.

2.7. Photocatalytic Hydrogen Production Tests. Photocatalytic H_2 production tests used a GEL-SPH2N photocatalytic activity evaluation system. Briefly, CTF-CN or g-C_3N_4 (25 mg) was dispersed in a H_2O : TEOA : CH_3OH solution (50 mL) with a volume ratio 85 : 10 : 5. To this dispersion, a certain amount of $K_2PtCl_6{\cdot}6H_2O$ was added (sufficient to achieve a Pt loading of 5 wt.%); then, the headspace of the reactor system purged with N_2 for 1 h under constant stirring. Next, the system was irradiated using a 300 W xenon lamp with a cut-off filter ($\lambda > 420$ nm), which resulted in the photocatalytic reduction of cationic Pt species to Pt^0. H_2 evolved during the Xe lamp irradiation was quantified by gas chromatography. An autosampler removed a small portion of the headspace gas every 30 min, which was then directly injected into a Shimadzu GC 2014 equipped with a TCD detector and Carboxen-1010 plot capillary column ($L \times$ I.D. = 30 m $\times$ 0.53 mm, average thickness 30 μm). H_2 evolution was quantified against an external calibration curve of peak area versus moles of H_2. Photocatalytic tests for each sample were carried out in triplicate.

3. Results and Discussion

3.1. Characterization of CTF-CN and the g-C_3N_4 Reference Photocatalyst. The chemical composition of the covalent triazine framework with cyano groups (CTF-CN) was first examined by bulk elemental analysis. From Figure 1, it can be shown that the repeat unit for the polymeric compound has the chemical formula $C_{54}H_{12}O_6N_{12}S_6$. The theoretical weight percentage for each element in the CTF-CN product is therefore C, 58.06 wt.%; H, 1.08 wt.%; O, 8.59 wt.%; N, 15.05 wt.%; and S, 17.22 wt.%. Elemental analysis revealed the following composition: C, 54.21 wt.%; H, 1.18 wt.%; O, 10.70 wt.%; N, 14.05 wt.%; S, 16.06 wt.%; Br, 3.01 wt.%; and Na, 0.78 wt.%. The results confirmed that CTF-CN was relatively pure with the correct chemical formula $C_{54}H_{12}O_6N_{12}S_6$, along with ~0.4 equivalents of NaBr and 1 equivalent of H_2O. Given that the CTF-CN synthesis was effectively a one pot reaction, this is a very acceptable product purity. ^{1}H NMR spectroscopy confirmed that the triazine units derived from TAPT had been successfully incorporated into the CTF-CN product (Figure S1) with the expected loss of the amino (-NH_2) group protons of TAPT through condensation reactions with the central anhydride oxygen of TBNDA. The g-C_3N_4 reference photocatalyst had the elemental composition C, 34.98 wt.%; H, 1.52 wt.%; N, 59.0 wt.%; and O, 4.5 wt.%, corresponding to a carbon normalized molecular formula of $C_{3.00}N_{4.34}H_{1.55}O_{0.29}$, which is typical for g-C_3N_4 compounds prepared from urea [3–6]. The data suggests that a g-C_3N_4 product is nitrogen-rich, with a significant fraction of the nitrogen having been protonated (as =NH-, -NH_2, or –NH_3^+) and a small amount of surface oxygen present as H_2O, -OH, or -CO_2H species. Energy-dispersive X-ray spectroscopy, FT-IR, and XPS analyses discussed below provided further chemical composition information about the CTF-CN and g-C_3N_4 products.

FT-IR spectra for CTF-CN, the building blocks of CTF-CN, and the g-C_3N_4 reference photocatalyst are shown in Figure 2(a). TBNDA was characterized by two intense C=O stretching modes at 1784 and 1730 cm^{-1}, associated with the dianhydride groups in the molecule. Bands below 650 cm^{-1} are associated with C-Br stretching and bending vibrations in the molecule. Na_2(i-mnt) showed a C≡N stretching mode at 2173 cm^{-1} and an intense Na-S stretching mode ~497 cm^{-1}. The peaks seen in the 3200-3450 cm^{-1} region are O-H stretching modes of water of crystallization. The FT-IR spectrum of TAPT was characterized by peaks at 3318 and 3205 cm^{-1}, which could readily be assigned to the two N-H stretching modes of the –NH_2 groups in the molecule [36]. An in-plane bending vibration for the primary amine groups is also seen at 1617 cm^{-1}. Other bands at 1604 and 1364 cm^{-1} seen in the FT-IR spectrum of TAPT are associated with molecular vibrations of the triazine ring. The triazine ring vibrations were also present in the FT-IR spectrum of CTF-CN. However, conspicuously absent in the spectrum of CTF-CN were the primary amine vibrations characteristic of TAPT, implying that these groups were removed by reaction on forming CTF-CN. The absence of the intense dianhydride C=O vibrations of TBNDA in the spectrum of the CTF-CN is consistent with the mechanism proposed in Figure 1, where the –NH_2 groups of TAPT react with the dianhydride groups of TBNDA in forming the CTF-CN molecular polymer. New C=O stretching modes appear in the region 1640-1680 cm^{-1} for CTF-CN, consistent with the formation of imide moieties. The presence of the band at 2215 cm^{-1} indicates that cyano groups were successfully incorporated into the CTF-CN polymer through reaction between the Na_2(i-mnt) and TBNDA units. The FT-IR spectrum of CTF-CN is thus in good accord with the structure depicted in Figure 1 for the polymer. The FT-IR spectrum of the g-C_3N_4 reference photocatalyst was in good accord with prior literature reports, showing molecular vibrations associated with the heptazine units in the polymeric compound.

Powder X-ray diffraction data for CTF-CN, the chemical building blocks used in the synthesis of CTF-CN, and the g-C_3N_4 reference photocatalyst are shown in Figure 2(b). The TBNDA, Na_2(i-mnt), and TAPT building blocks were all crystalline solids, whereas the CTF-CN product was

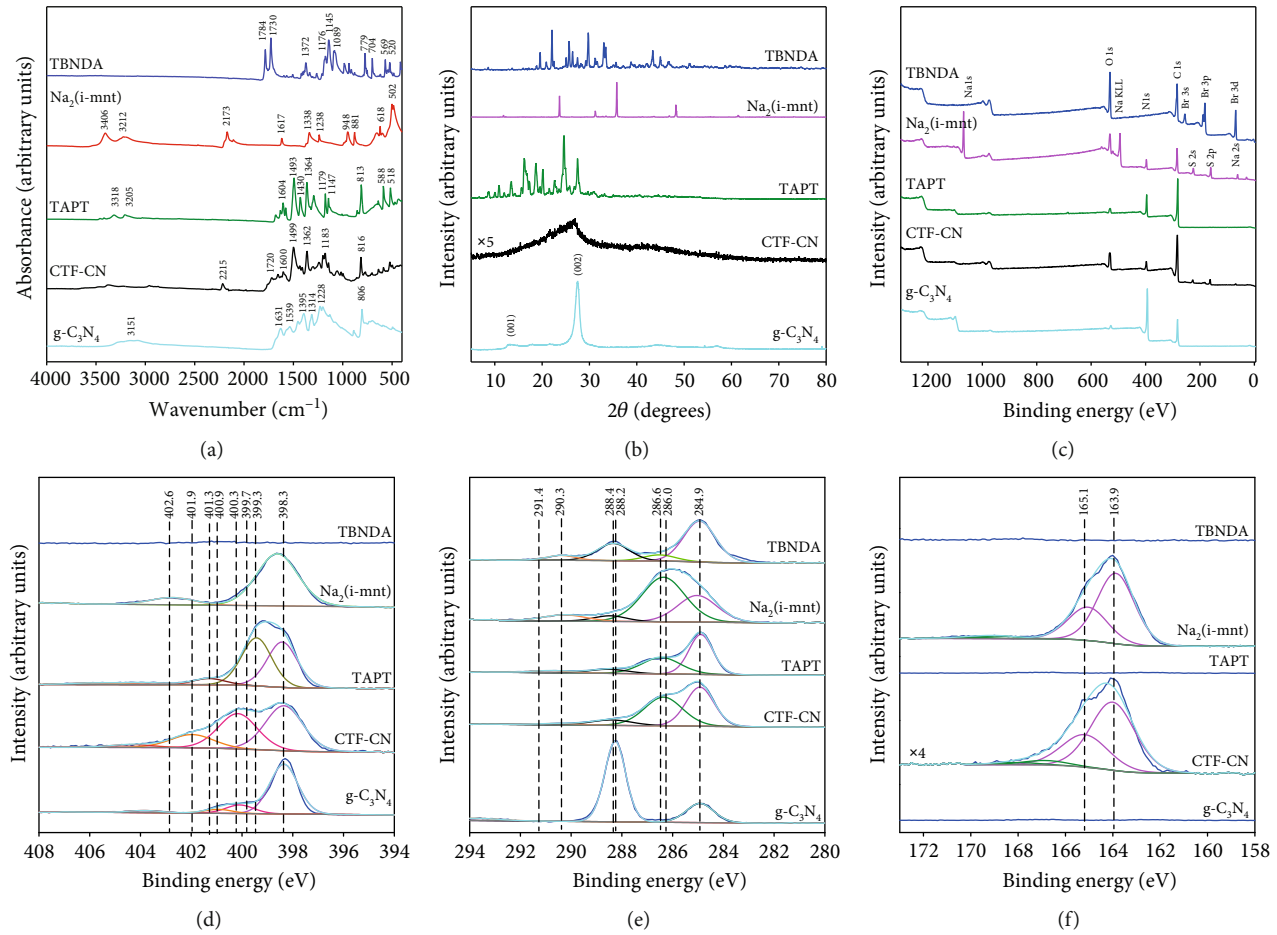

FIGURE 2: (a) FT-IR absorbance spectra for CTF-CN, the starting materials used in the synthesis of CTF-CN, and the g-C_3N_4 reference photocatalyst; (b) powder X-ray diffraction patterns for CTF-CN, the starting materials used in the synthesis of CTF-CN, and the g-C_3N_4 reference photocatalyst; (c–f) XPS data for CTF-CN, the g-C_3N_4 photocatalyst, and various reference compounds: (c) survey spectra; (d) N 1s region; (e) C 1s region; (f) S 2p region.

amorphous, characterized by a broad XRD feature with a maximum around $2\theta = 26^\circ$, which is tentatively attributed to π-π interactions between two dimensional polymeric chains. The lack of crystallinity in CTF-CN was supported by the absence of lattice fringes in the TEM images of Figures 3(c) and 3(d). The fact that CTF-CN was not crystalline is not surprising, since the structure of the framework (Figure 1) allows considerable rotation around the C-C bonds in the TAPT-derived component (i.e., the bonds between the triazine rings and aromatic rings). The g-C_3N_4 reference photocatalyst showed characteristic XRD peaks at $2\theta = 12.8^\circ$ and 27.3° which could readily be assigned to the (001) and (002) reflections, respectively, of crystalline multilayered g-C_3N_4.

X-ray photoelectron spectroscopy was applied to probe the near-surface region chemical composition of CTF-CN, the building blocks of CTF-CN, and the g-C_3N_4 reference photocatalyst, as well as to examine the nitrogen speciation in these materials. XPS survey spectra for the different samples are shown in Figures 2(c)–2(f). Near-surface region chemical compositions for each sample are summarized in Table S1. The near-surface region chemical compositions for most of the materials differed from their bulk composition due to the adsorption of adventitious hydrocarbons ($C_xH_yO_z$), which resulted in an overestimation of the carbon and oxygen contents in the samples (XPS does not detect H). For TBNDA, the O : Br ratio was 3 : 2, in good agreement with theory. For Na_2(i-mnt), the Na : S : N ratio was ~1 : 1 : 1, again in good agreement with expectations. For CTF-CN, the N : S ratio was 2 : 1, in good accord with the bulk elemental analysis results. The presence of some surface Br was also found by XPS for CTF-CN, which was also in accord with the bulk elemental analysis results (likely present as a minor NaBr impurity or simply adsorbed bromide ions). High-resolution narrow scans were also collected over the N 1s, C 1s, and S 2p regions of the samples (Figures 2(d)–2(f), respectively). The N 1s spectrum of CTF-CN was deconvoluted into 3 components with binding energies of 398.3, 400.3, and 401.9 eV. By comparison with previous XPS literature for covalent triazine frameworks and related N-heterocyclic compounds (Table S2) [37, 38], these peaks can readily be assigned to pyridinic (C-N=C), imidic (C-N-C=O), and cyano (-C≡N) groups, respectively. Based on the structure shown in Figure 1 for CTF-CN, the area ratio of the 398.3 :

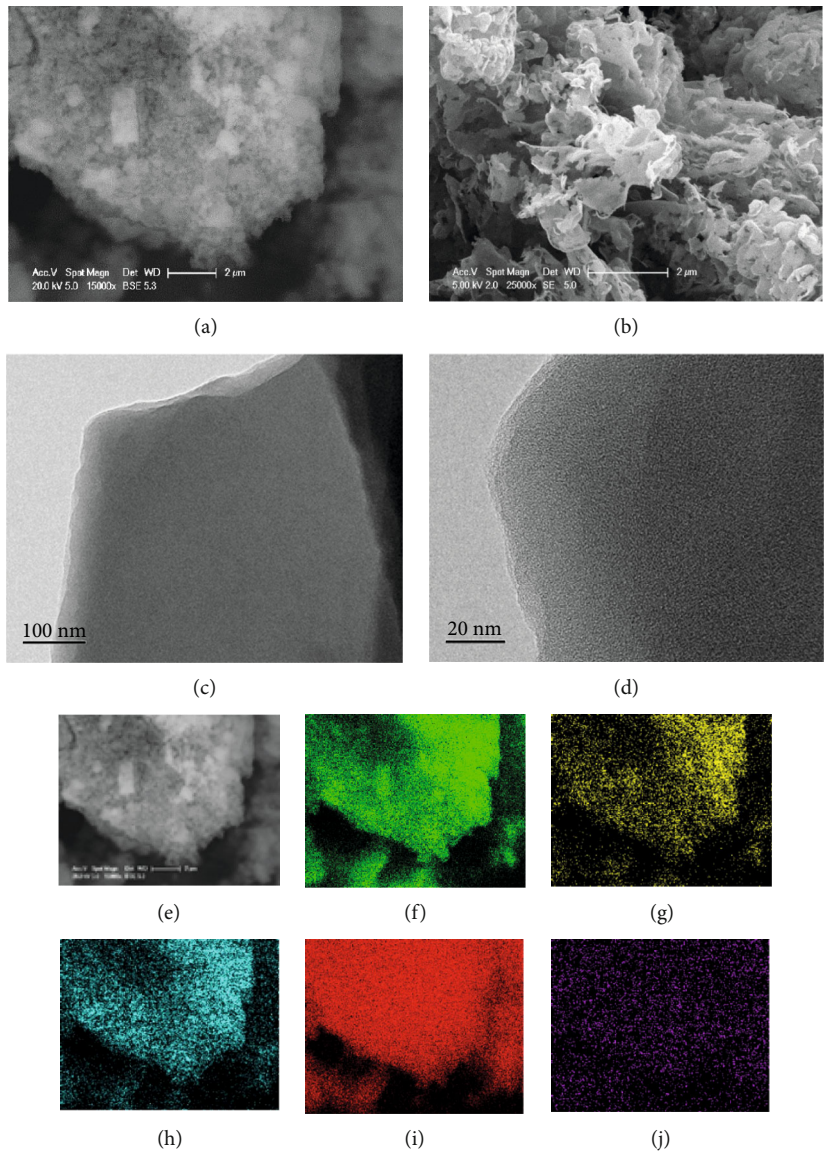

FIGURE 3: (a) SEM image of CTF-CN, (b) SEM image of g-C_3N_4, and (c, d) TEM images of CTF-CN and (e) secondary electron image and (f–j) energy-dispersive spectroscopy element maps for CTF-CN. Elements mapped were (f) C, (g) N, (h) O, (i) S, and (j) Br.

400.4 : 401.9 eV peaks should be 1 : 1 : 2. The experimental area ratio determined from Figure 2(d) was 1 : 1 : 0.5, implying that the near-surface region concentration of cyano groups was ~25% of the theoretical value. This can easily be rationalized by taking into account the susceptibility of cyano groups to hydrolysis, resulting in the production of surface amide or even carboxyl moieties (i.e., $-C \equiv N + H_2O \longrightarrow C[O]\text{-}NH_2$, then $C[O]\text{-}NH_2 + H_2O \longrightarrow C[O]\text{-}OH + NH_3$). The C 1s spectrum of CTF-CN contained components at 284.9, 286.0, and 288.4 eV, which can be assigned to carbon in aromatic rings/adventitious hydrocarbons (i.e., aromatic sp^2 and sp^3 carbons), C-N/-C≡N/C-S species (all of which have similar binding energies), and N-C=N or N-C=O species, respectively (Table S3) [38]. The S 2p spectrum of CTF-CN showed two peaks at 163.9 and 165.1 eV in a 2 : 1 area ratio (S $2p_{3/2}$ and S $2p_{1/2}$, respectively), with identical peaks being observed in the S 2p spectrum of the Na_2(i-mnt) starting material. The observation of these peaks in the S 2p spectrum of CTF-CN provides further experimental evidence for the successful attachment of the i-mnt groups onto the TBNDA units in the framework. Taking into account the surface reactivity of the cyano groups and the adsorption of adventitious hydrocarbons, it can be concluded that the XPS data collected for CTF-CN was in reasonable accord with expectations. The N 1s spectrum of the g-C_3N_4 reference photocatalyst showed peaks at 398.3 eV and 400.0 eV, which can easily be assigned to C-N=C and C-NH-C species [39]. Further weaker peaks at 400.9 and 403.6 eV are assigned to graphitic N and $\pi \longrightarrow \pi^*$ transitions, respectively. The C 1s spectrum of g-C_3N_4 was dominated by at intense peak at 288.2 eV which can readily be assigned to N-C=N species in the heptazine units of g-C_3N_4. The peak at 284.9 eV is due to adventitious hydrocarbons, whilst $\pi \longrightarrow \pi^*$ transitions give rise to weak features around 293-294 eV.

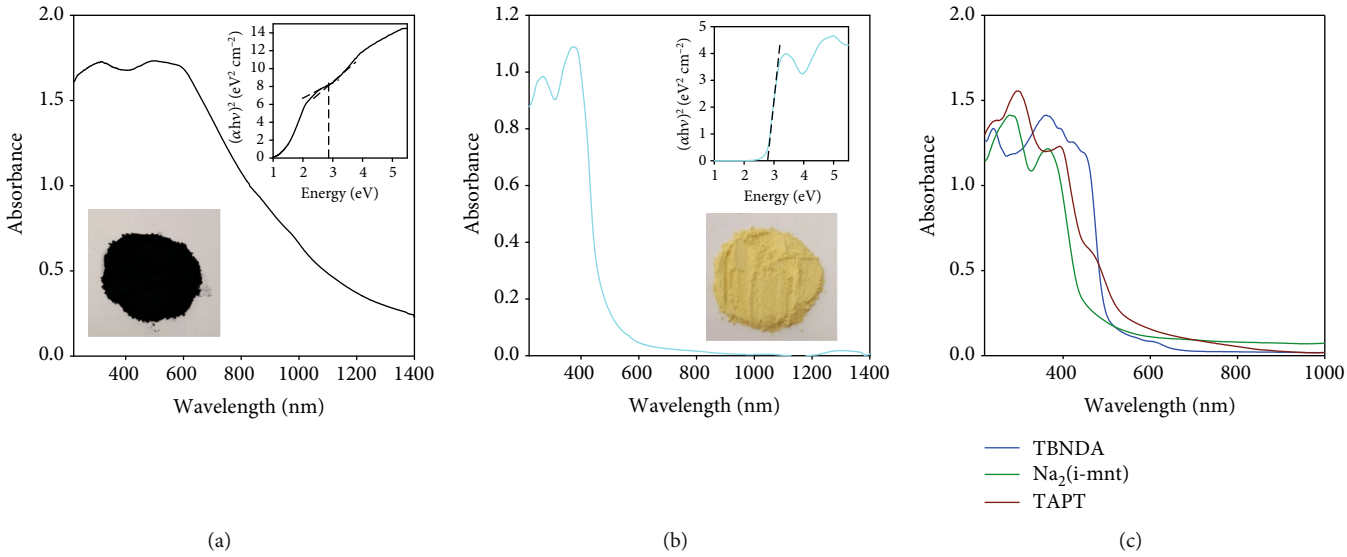

FIGURE 4: UV-vis absorbance spectra, Tauc plots, and digital photographs for (a) CTF-CN and (b) the g-C_3N_4 reference photocatalyst. For the Tauc analyses, it was assumed that both CTF-CN and g-C_3N_4 are direct band gap semiconductors. (c) Comparison of the UV-vis absorbance spectra for TBNDA, Na_2(i-mnt), and TAPT.

Scanning electron microscopy (SEM) and transmittance electron microscopy (TEM) were applied to examine the morphologies of the CTF-CN and g-C_3N_4 products (Figures 3(a) and 3(b)). The as-prepared CTF-CN sample was found to consist of thin 2D sheets, with the sheets having a small lateral size and haphazardly assembled into 3D bundles (Figure 3(a)). These bundles could quite easily be broken up by ultrasonication, with TEM analysis revealing the CTF-CN sheets to be very thin, suggesting that they possessed some form of loosely layered structure to achieve thicknesses of a few nanometers. The g-C_3N_4 reference photocatalyst similarly had a characteristic 2D sheet-like structure, with the lateral size of the g-C_3N_4 sheets being at least one order of magnitude larger than the CTF-CN nanosheets.

Energy-dispersive spectroscopy (EDS) was subsequently applied to examine the element dispersion in CTF-CN. As shown in Figures 3(e)–3(j), the sample showed a uniform distribution of C, N, O, and S, with trace amounts of Br also found. Quantitative EDS analysis revealed that the ratios of these elements were consistent with the molecular formula determined from the bulk elemental analysis (i.e., $C_{54}H_{12}O_6N_{12}S_6$ with a small amount of Na, Br, and O).

Surface area and porosity are important considerations when developing photocatalytic materials. N_2 physisorption data was collected at 77 K for both CTF-CN and g-C_3N_4. Nitrogen adsorption-desorption isotherms collected for CTF-CN are shown in Figure S2. The CTF-CN sample showed a type II adsorption isotherm under the IUPAC classification system. The BET specific surface area was determined to be 96 $m^2 g^{-1}$, which was low compared to areas reported for other crystalline CTF materials. It can therefore be concluded that CTF-CN does not possess an ordered microporous or ordered mesoporous structure, consistent with the XRD analysis which showed the material to be amorphous. A further possible reason for the modest specific surface may be blocking of pores by the abundant cyano groups in the CTF-CN structure. The BET specific surface area for the g-C_3N_4 reference photocatalyst was 108.3 $m^2 g^{-1}$. The similarity in surface area between CTF-CN and g-C_3N_4 was desirable here, as it meant that both samples would offer almost the same amount of surface for light absorption and surface redox reactions during the photocatalytic tests.

UV-vis transmittance spectra and Tauc plots for CTF-CN and g-C_3N_4 are shown in Figures 4(a) and 4(b). CTF-CN was black, absorbing very strongly across the whole visible spectrum. Such a wide absorption range was not surprising, given the fact the polymer contained multiple chromophores with accessible $\pi \longrightarrow \pi^*$ and $n \longrightarrow \pi^*$ transitions (the absorption spectra for the TBNDA, Na_2(i-mnt), and TAPT are shown in Figure 4(c) for comparison). The g-C_3N_4 reference photocatalyst had a characteristic absorption edge ~450 nm and an absorption tail extending to longer wavelengths associated with nitrogen defects. Band gap energies extrapolated from the Tauc plots for CTF-CN and g-C_3N_4 were ~2.8 eV (due to the many different chromophores in the CTF-CN polymer, exact determination of E_g was challenging) and 2.7 eV, respectively. It is likely that the E_g value needed to drive the H_2 production reactions using CTF-CN is probably similar to that of g-C_3N_4 (i.e., ~2.7-2.8 eV). This implies that the separation between the CB and the VB (or alternatively the separation between S_1 and S_0 states) was very similar in the two materials.

For many applications involving covalent triazine frameworks, thermal stability is important. Figure S3 shows thermogravimetric (TGA) data for TBNDA, Na_2(i-mnt), TAPT, and CTF-CN collected with heating under a N_2 atmosphere. Except for Na_2(i-mnt), which showed a large mass loss below 100°C due to the loss of water of crystallization (3 equivalents of H_2O per Na_2(i-mnt)), all

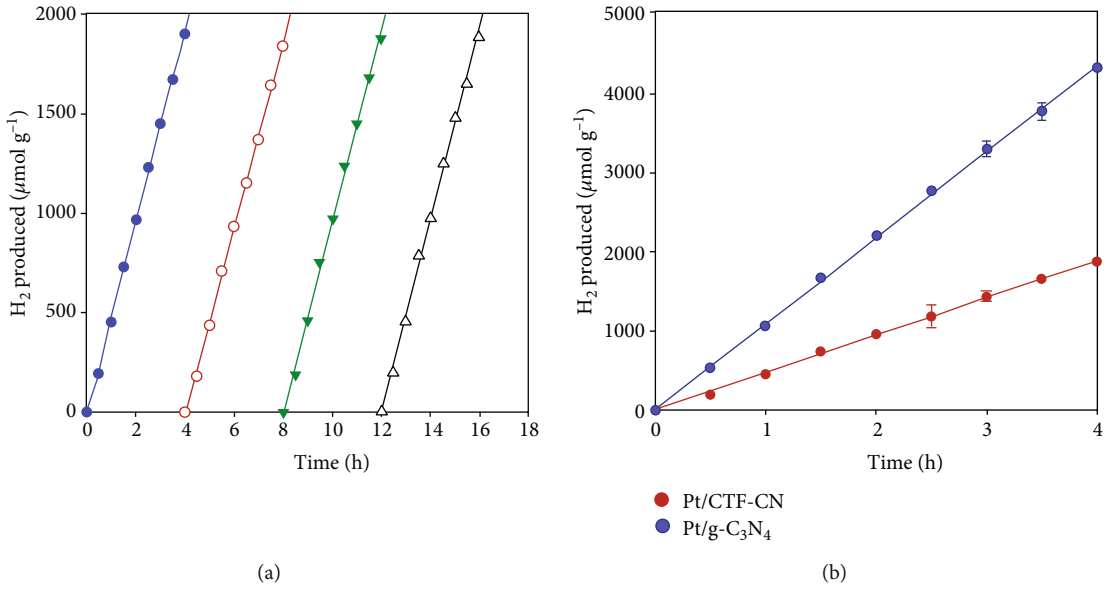

FIGURE 5: (a) H_2 production data for Pt/CTF-CN over four successive testing cycles in a H_2O/TEOA/CH_3OH (85 : 10 : 5 by volume) mixture under irradiation from a 300 W Xenon lamp and (b) plots of H_2 production versus time for Pt/CTF-CN and the Pt/g-C_3N_4 reference photocatalyst.

samples were stable to temperatures above 300°C. It can be concluded that CTF-CN is thermally very stable.

3.2. Photocatalytic Hydrogen Production Tests. Following the detailed physicochemical characterization studies of CTF-CN and g-C_3N_4 described above, we then focussed on evaluating the photocatalytic hydrogen production performance of these two materials in aqueous media. In a typical experiment, CTF-CN or g-C_3N_4 (25 mg) was dispersed in 50 mL of a H_2O : TEOA : CH_3OH mixture (containing 10 vol% TEOA and 5 vol% CH_3OH). The H_2O : TEOA : CH_3OH solution contained sufficient $K_2PtCl_6 \cdot 6H_2O$ to achieve a Pt metal loading of 5 wt.% once all the dissolved platinum salt had been reduced. The catalyst dispersions were stirred in the dark under a N_2 flow for 1 h to remove any dissolved oxygen, then irradiated by a 300 W Newport Xe light source with a 420 nm cutoff filter. This resulted in the simultaneous formation of Pt metal nanoparticles on the surface of the catalysts (see characterization data below) and concurrent H_2 evolution.

Figure 5(a) shows plots of H_2 production over time for the Pt/CTF-CN photocatalyst. The photocatalytic H_2 production test was carried out over a 4 h period, affording a H_2 production rate of 484.7 μmol g^{-1} h^{-1} for run #1 (see Table S4). The reactor was then shielded from the Xe lamp and purged with N_2 for 15 min, then again irradiated with the Xe lamp for 4 h. The H_2 production rate for run #2 was 468.4 μmol g^{-1} h^{-1} and 481.3 and 479.9 μmol g^{-1} h^{-1} for the two subsequent runs (i.e., runs #3 and #4). It can therefore be concluded that the Pt/CTF-CN photocatalyst was extremely stable under the applied testing conditions, with no loss in activity observed over a 16 h testing period. Figure 5(b) compares the performance of the Pt/CTF-CN and Pt/g-C_3N_4 photocatalysts over the 4 repeat test cycles (the Pt/g-C_3N_4 photocatalyst also showed no change in activity over the 4 cycles). The hydrogen production rate over the Pt/g-C_3N_4 photocatalyst was 1088 μmol g^{-1} h^{-1} or approximately twice that of Pt/CTF-CN when the rates were normalized by the specific surface area (10.054 μmol m^{-2} h^{-1} for Pt/g-C_3N_4 versus 4.985 μmol m^{-2} h^{-1} for Pt/CTF-CN). Benchmarking using the g-C_3N_4 reference photocatalyst, which is relatively easy to synthesize, provides a useful indicator of the merits of the Pt/CTF-CN photocatalyst for H_2 production. With optimization of parameters such as metal cocatalyst loading and Pt/CTF-CN dispersion, it is likely that the performance of the Pt/CTF-CN could be improved to the level of the 5 wt.% Pt/g-C_3N_4 photocatalyst. Table S5 compares the performance of the Pt/CTF-CN photocatalyst for H_2 production with various other covalent triazine framework photocatalysts and CTF hybrid photocatalysts. The data shows that the H_2 production activity of Pt/CTF-CN photocatalyst sits in the middle of the range of reported values for CTF-based photocatalysts. Again, we urge caution in comparing the activity of Pt/CTF-CN with the other systems, due to differences in cocatalyst loading content, sacrificial agent, presence/absence of cyano groups, and various other parameters which can all influence H_2 production rates as shown in Figure S4. However, it should be noted that under the same experimental conditions, the hydrogen production rate of Pt/CTF-CN was nearly four times that of Pt/CTF (without cyano groups), indicating that the presence of cyano groups can promote the efficient separation of photogenerated electrons and holes in covalent triazine frameworks.

Here, we strongly advocate that researchers in the field test a Pt/g-C_3N_4 photocatalyst alongside their Pt/CTF or Pt/CTF-CN photocatalysts to allow meaningful comparison of the work of different groups (measurement of apparent quantum yields is an alternative approach that allows the work of different groups to be compared, though in our

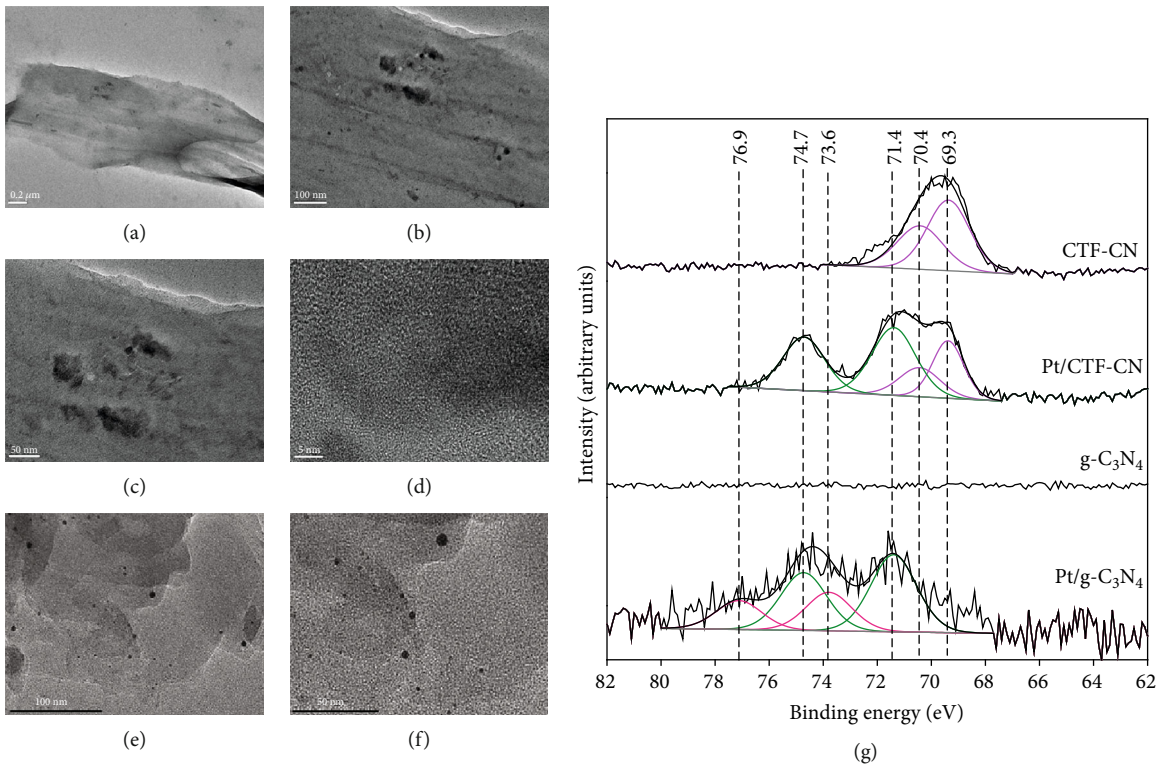

FIGURE 6: TEM images for (a–d) Pt/CTF-CN following the H_2 production tests and (e, f) Pt/g-C_3N_4. The Pt nanoparticles were formed by the photoreduction of hexachoroplatinate ions in a H_2O/TEOA/CH_3OH (85 : 10 : 5 by volume) mixture with photocatalyst exposure to a 300 W Xe lamp. (g) Pt 4f XPS spectra for CTF-CN, Pt/CTF-CN, g-C_3N_4, and Pt/g-C_3N_4. For the CTF-CN and Pt/CTF-CN, the Br 3d peaks also appear in this spectral region (for the curve fits, pink = Br 3d, green = Pt^0, and red = Pt^{2+}).

experience is less straightforward than just measuring a simple reference catalyst under the same testing conditions). For the interest of readers, Table S6 compares the activity of our Pt/g-C_3N_4 photocatalyst for H_2 production with prior literature reports for Pt/g-C_3N_4 systems.

Regarding the role of the Pt cocatalyst, negligible H_2 production was observed from CTF-CN or g-C_3N_4 in the absence of $K_2PtCl_6{\cdot}6H_2O$ addition. Clearly, the surfaces of these materials have high overpotentials for H_2 evolution. $K_2PtCl_6{\cdot}6H_2O$ was therefore added to the system to produce the Pt^0 nanoparticles by photoreduction. When the Xe lamp irradiates the photocatalyst dispersion containing Pt(II) ions, photogenerated electrons are easily transferred from the photocatalyst to surface-adsorbed Pt(II) ions, resulting in the reduction of Pt(II) to Pt^0. Pt nanoparticles created on the photocatalyst surface then act as efficient hydrogen evolution sites since platinum has a high work function ($\Phi = 5.65$ eV) and a low Fermi level (i.e., a Schottky junction is formed between the photocatalyst and Pt). As a result, electrons photogenerated in the photocatalyst migrate onto the Pt nanoparticles, providing cathodic sites for H_2 generation and suppressing electron-hole pair recombination. Electron-hole pair recombination was further suppressed here by using triethanolamine (TEOA) and methanol as sacrificial hole scavengers (electron donors). Figures 6(a)–6(d) show TEM images for the Pt/CTF-CN photocatalyst after the four successive cycles of H_2 production tests depicted in Figure 5(a). Following, the tests, Pt nanoparticles can be seen on the surface of the CTF-CN photocatalyst, ranging in size from 1 to 10 nm. In addition, some lattice fringes can be seen in high-resolution images (Figure 6(d)), which may be due to Pt nanoparticles or possibly due to partial crystallization of the CTF-CN during the photoreaction. For the Pt/g-C_3N_4 photocatalyst, which offered a larger atomic number contrast between Pt and the support, the Pt nanoparticles were easier to discern, having sizes ranging from 1 to 8 nm (Figures 6(e)–6(f)). ICP-MS confirmed that the Pt/CTF-CN and Pt/g-C_3N_4 photocatalysts had Pt loadings in the range 4.6-4.8 wt.%, in good accord with the nominal target loading of 5 wt.%. Pt 4f XPS spectra for the Pt/CTF-CN and Pt/g-C_3N_4 photocatalysts are shown in Figure 6(g). For the Pt/CTF-CN photocatalyst, the Pt 4f spectrum showed peaks at 71.4 and 76.9 eV in a 4 : 3 area ratio, which can readily be assigned to the Pt $4f_{7/2}$ and $4f_{5/2}$ signals of platinum metal (peaks at 69.3 and 70.4 eV in a 3 : 2 area ratio are Br $3d_{5/2}$ and Br $3d_{3/2}$ peaks, respectively, of a surface bromide impurity). For Pt/g-C_3N_4, two sets of Pt peaks are seen; the peaks at 71.2 and 76.7 eV are due to Pt^0, whereas the peaks at 73.6 and 76.9 eV are due to Pt(II). The TEM and XPS data for Pt/CTF-CN and Pt/g-C_3N_4 thus confirm the in situ reduction of Pt(II) ions to Pt^0 on the surface of the photocatalysts under the conditions of the H_2 production tests. FT-IR spectra for CTF-CN and Pt/CTF-CN (after 16 h of H_2 production testing) are shown in Figure S5. Following the tests, new peaks appear at 3270

and 1036 cm^{-1}, consistent with the introduction of surface C-O-H groups. The introduction of these groups does not appear to adversely impact the photocatalytic activity of Pt/CTF-CN, since the H_2 production rate did not change over the 16 h of testing (Table S4). Currently, we are performing apparent quantum yield experiments using narrow band pass filters on Pt/CTF-CN to explore the relationship between the CTF-CN electronic structure and photocatalytic H_2 performance.

3.3. Alternative Microwave-Assisted Synthesis of CTF-CN. Finally, we explored an alternative microwave-based synthesis of CTF-CN. It was hypothesized that by using microwave heating, the kinetics of CTF-CN synthesis could be enhanced, as has been observed by other groups [40, 41]. Under a nitrogen atmosphere, TBNDA and Na_2(i-mnt) were added to a round bottomed three-necked flask, with DMF added as the solvent. The flask was then heated at 50°C for 1 h in an oil bath, after which TAPT was added to suspension. Next, the mixture was transferred to a microwave reactor, then subjected to 300 W microwave irradiation for 30 min. The reaction temperature achieved was ~70°C. Following the treatment, the contents of the microwave reactor were poured into ice-cold ethanol, then centrifuged to obtain the CTF-CN product. The microwave-synthesis method had a low yield (~10% due to the relatively short reaction time, compare 90% for the solvothermal synthesis over 5 d), though giving a CTF-CN polymer with a much more uniform sheet-like structure than the solvothermal method (i.e., a structure more comparable to g-C_3N_4), as shown in Figure S6. Currently, we are evaluating the performance of the microwave-assisted synthesized CTF-CN for photocatalytic hydrogen production. We are also exploring microwave-assisted synthetic approaches for postsynthetic modification of CTF-CN by taking advantage of the reactivity of the cyano groups in the polymer.

4. Conclusion

A novel covalent triazine framework functionalized with numerous cyano groups was successfully synthesized using both solvothermal and microwave-assisted methods. The CTF-CN polymer absorbed strongly across the visible region and after decoration with Pt nanoparticles demonstrated very good activity for photocatalytic hydrogen production in a H_2O-TEOA-CH_3OH mixture under UV-vis excitation. A hydrogen production rate of ~487.6 $\mu mol\, g^{-1}\, h^{-1}$ was realized at a Pt loading of 5 wt.%, comparable to that of a Pt/g-C_3N_4 photocatalyst under the same testing conditions (1088.8 $\mu mol\, g^{-1}\, h^{-1}$). The CTF-CN demonstrated excellent thermal and photocatalytic stability, with no deactivation observed even after 16 h testing. In addition, the presence of the rich cyano groups on the skeleton of CTF-CN provides an abundance of active sites for further chemical modifications, thus potentially allowing the synthesis of families of CTFs using CTF-CN as an intermediate for further applications such as electrocatalyst development for fuel cells and batteries [42, 43].

Data Availability

The original data used to support the findings of this study are available from the corresponding author upon request.

Conflicts of Interest

The authors declare that they have no conflicts of interest.

Acknowledgments

This work was supported by the National Key R&D Plan (No. 2016YFB0302400) and Agricultural Key Applied Technology Innovation Project of Shandong Province (2017, No. 6). GINW acknowledges funding support from the Shandong Provincial "Double-Hundred Talent Plan" on 100 Foreign Experts, the Energy Education Trust of New Zealand, and the MacDiarmid Institute for Advanced Materials and Nanotechnology.

Supplementary Materials

Figure S1: ^1H NMR spectra for (a) TAPT and (b) CTF-CN. The samples were dissolved in deuterated DMSO for the analyses. Figure S2: N_2 adsorption and desorption isotherms for CTF-CN collected at 77 K. Table S1: summarized XPS chemical composition data for CTF-CN, its precursors, and g-C_3N_4 reference photocatalyst. Data for Pt/CFT-CN and Pt/g-C3N4 is also included. Table S2: N 1s peak position for different N environments. Table S3: C 1s peak position for different C environments. Figure S3: TGA data for CTF-CN and the starting materials used in the synthesis of CTF-CN. All data was collected at a heating rate of 10°C min^{-1} under a N_2 atmosphere. Table S4: summarized H_2 production data for Pt/CTF-CN and Pt/g-C_3N_4 photocatalysts. Table S5: performance comparison of different covalent triazine framework- (CTF-) based photocatalysts for H_2 production under visible ($\lambda > 420$ nm) or UV-visible irradiation. Figure S4: (a) H_2 production data for CTF-CN with different cocatalyst Pt contents, (b) H_2 production data for CTF-CN with different sacrifices, and (c) H_2 production data for CTF-CN and CTF (without cyano groups). Figure S5: FT-IR absorbance spectra for CTF-CN and g-C_3N_4 before and after the H_2 production tests. During the H_2 production tests, aqueous Pt(II) was photoreduced to Pt^0 on the surface of the photocatalyst. Table S6: summarized H_2 production data for various Pt/g-C_3N_4 photocatalysts. Figure S6: TEM images of CTF-CN synthesized using the microwave method. *(Supplementary Materials)*

References

[1] X. Wang, K. Maeda, A. Thomas et al., "A metal-free polymeric photocatalyst for hydrogen production from water under visible light," *Nature Materials*, vol. 8, no. 1, pp. 76–80, 2009.

[2] G. Liao, Y. Gong, L. Zhang, H. Gao, G. J. Yang, and B. Fang, "Semiconductor polymeric graphitic carbon nitride photocatalysts: the "holy grail" for the photocatalytic hydrogen evolution reaction under visible light," *Energy & Environmental Science*, vol. 12, no. 7, pp. 2080–2147, 2019.

[3] S. Cao and J. Yu, "g-C_3N_4-based photocatalysts for hydrogen generation," *The Journal of Physical Chemistry Letters*, vol. 5, no. 12, pp. 2101–2107, 2014.

[4] J. Liu, Y. Zhang, L. Lu, G. Wu, and W. Chen, "Self-regenerated solar-driven photocatalytic water-splitting by urea derived graphitic carbon nitride with platinum nanoparticles," *Chemical Communications*, vol. 48, no. 70, pp. 8826–8828, 2012.

[5] P. Niu, M. Qiao, Y. Li, L. Huang, and T. Zhai, "Distinctive defects engineering in graphitic carbon nitride for greatly extended visible light photocatalytic hydrogen evolution," *Nano Energy*, vol. 44, pp. 73–81, 2018.

[6] C.-Q. Xu, K. Li, and W.-D. Zhang, "Enhancing visible light photocatalytic activity of nitrogen-deficient g-C_3N_4 via thermal polymerization of acetic acid-treated melamine," *Journal of Colloid and Interface Science*, vol. 495, pp. 27–36, 2017.

[7] J. Liu, Y. Liu, N. Liu et al., "Water splitting. Metal-free efficient photocatalyst for stable visible water splitting via a two-electron pathway," *Science*, vol. 347, no. 6225, pp. 970–974, 2015.

[8] Y. Yu, W. Yan, X. Wang et al., "Surface engineering for extremely enhanced charge separation and photocatalytic hydrogen evolution on g-C_3N_4," *Advanced Materials*, vol. 30, no. 9, article 1705060, 2018.

[9] Y.-J. Yuan, Z. Shen, S. Wu et al., "Liquid exfoliation of g-C_3N_4 nanosheets to construct 2D-2D MoS_2/g-C_3N_4 photocatalyst for enhanced photocatalytic H_2 production activity," *Applied Catalysis B: Environmental*, vol. 246, pp. 120–128, 2019.

[10] S. Anandan, J.-J. Wu, D. Bahnemann, A. Emeline, and M. Ashokkumar, "Crumpled Cu_2O-g-C_3N_4 nanosheets for hydrogen evolution catalysis," *Colloids and Surfaces A: Physicochemical and Engineering Aspects*, vol. 527, pp. 34–41, 2017.

[11] W.-J. Ong, L.-L. Tan, Y.-H. Ng, S.-T. Yong, and S.-P. Chai, "Graphitic carbon nitride (g-C_3N_4)-based photocatalysts for artificial photosynthesis and environmental remediation: are we a step closer to achieving sustainability?," *Chemical Reviews*, vol. 116, no. 12, pp. 7159–7329, 2016.

[12] Z. Jiang, X. Zhang, H.-S. Chen, X. Hu, and P. Yang, "Formation of g-C3N4Nanotubes towards superior photocatalysis performance," *ChemCatChem*, vol. 11, no. 18, pp. 4558–4567, 2019.

[13] P. Kuhn, M. Antonietti, and A. Thomas, "Ionothermalsynthese von porösen kovalenten Triazin-Polymernetzwerken," *Angewandte Chemie*, vol. 120, no. 18, pp. 3499–3502, 2008.

[14] A.-P. Cote, A.-I. Benin, N.-W. Ockwig, M.-O. Keeffe, A.-J. Matzger, and O.-M. Yaghi, "Porous, crystalline, covalent organic frameworks," *Science*, vol. 310, no. 5751, pp. 1166–1170, 2005.

[15] D. Chen, S. Huang, L. Zhong et al., "In situ preparation of thin and rigid COF film on Li anode as artificial solid electrolyte interphase layer resisting Li dendrite puncture," *Advanced Functional Materials*, vol. 30, no. 7, article 1907717, 2020.

[16] G. Wang, N. Tahir, I. Onyshchenko et al., "Novel hexaazatrinaphthalene-based covalent triazine frameworks as high- performance platforms for efficient carbon capture and storage," *Microporous and Mesoporous Materials*, vol. 290, article 109650, 2019.

[17] Z. Yang, S. Wang, Z. Zhang et al., "Influence of fluorination on CO2adsorption in materials derived from fluorinated covalent triazine framework precursors," *Journal of Materials Chemistry A*, vol. 7, no. 29, pp. 17277–17282, 2019.

[18] P. van der Voort, H.-S. Jena, C. Krishnaraj, J. Schmidt, K. Leus, and K. Van Hecke, "Triggering white-light emission in a 2D imine covalent organic framework through lanthanide augmentation," *ACS Applied Materials & Interfaces*, vol. 11, no. 30, pp. 27343–27352, 2019.

[19] K. Kamiya, R. Kamai, K. Hashimoto, and S. Nakanishi, "Platinum-modified covalent triazine frameworks hybridized with carbon nanoparticles as methanol-tolerant oxygen reduction electrocatalysts," *Nature Communications*, vol. 5, no. 1, pp. 1–6, 2014.

[20] S.-y. Ding, J. Gao, Q. Wang et al., "Construction of covalent organic framework for catalysis: Pd/COF-LZU1 in Suzuki–Miyaura coupling reaction," *Journal of the American Chemical Society*, vol. 133, no. 49, pp. 19816–19822, 2011.

[21] G. Zhang, Z.-a. Lan, and X. Wang, "Conjugated polymers: catalysts for photocatalytic hydrogen evolution," *Angewandte Chemie International Edition*, vol. 55, no. 51, pp. 15712–15727, 2016.

[22] J. Xie, S.-A. Shevlin, Q. Ruan et al., "Efficient visible light-driven water oxidation and proton reduction by an ordered covalent triazine-based framework," *Energy & Environmental Science*, vol. 11, no. 6, pp. 1617–1624, 2018.

[23] T. Banerjee, K. Gottschling, G. Savasci, C. Ochsenfeld, and B.-V. Lotsch, "H_2 evolution with covalent organic framework photocatalysts," *ACS Energy Letters*, vol. 3, no. 2, pp. 400–409, 2018.

[24] C. B. Meier, R. S. Sprick, A. Monti et al., "Structure-property relationships for covalent triazine-based frameworks: the effect of spacer length on photocatalytic hydrogen evolution from water," *Polymer*, vol. 126, pp. 283–290, 2017.

[25] J. Bi, W. Fang, L. Li et al., "Covalent triazine-based frameworks as visible light Photocatalysts for the splitting of water," *Macromolecular Rapid Communications*, vol. 36, no. 20, pp. 1799–1805, 2015.

[26] J. H. Ko, N. Kang, N. Park et al., "Hollow microporous organic networks bearing triphenylamines and anthraquinones: diffusion pathway effect in visible light-driven oxidative coupling of benzylamines," *ACS Macro Letters*, vol. 4, no. 7, pp. 669–672, 2015.

[27] L. Li, W. Fang, P. Zhang, Y. He, J. Wang, and W. Su, "Sulfur-doped covalent triazine-based frameworks for enhanced photocatalytic hydrogen evolution from water under visible light," *Journal of Materials Chemistry A*, vol. 4, no. 32, pp. 12402–12406, 2016.

[28] L. Wang, Y. Hong, E. Liu, X. Duan, X. Lin, and J. Shi, "A bottom-up acidification strategy engineered ultrathin g-C_3N_4 nanosheets towards boosting photocatalytic hydrogen evolution," *Carbon*, vol. 163, pp. 234–243, 2020.

[29] M. Sun, H. X. Guan, W. D. Zhang, and Y. X. Yu, "Strong organic acid-assistant synthesis of holey graphitic carbon nitride for efficient visible light photocatalytic H_2 generation," *International Journal of Hydrogen Energy*, vol. 44, no. 41, pp. 23091–23100, 2019.

[30] J. Wen, J. Xie, X. Chen, and X. Li, "A review on g-C_3N_4-based photocatalysts," *Applied Surface Science*, vol. 391, pp. 72–123, 2017.

[31] Y. Hu, Y. Qin, X. Gao et al., "One-pot synthesis of core-expanded naphthalene diimides: enabling N-substituent modulation for diverse n-type organic materials," *Organic Letters*, vol. 14, no. 1, pp. 292–295, 2012.

[32] Y. Hu, X. Gao, C.-A. Di et al., "Core-expanded naphthalene diimides fused with sulfur heterocycles and end-capped with electron-withdrawing groups for air-stable solution-

processed n-channel organic thin film transistors," *Chemistry of Materials*, vol. 23, no. 5, pp. 1204–1215, 2011.

[33] X. Gao, C.-a. Di, Y. Hu et al., "Core-expanded naphthalene diimides fused with 2-(1, 3-dithiol-2-ylidene) malonitrile groups for high-performance, ambient-stable, solution-processed n-channel organic thin film transistors," *Journal of the American Chemical Society*, vol. 132, no. 11, pp. 3697–3699, 2010.

[34] F. Jing, R. Liang, J. Xiong et al., "MIL-68(Fe) as an efficient visible-light-driven photocatalyst for the treatment of a simulated waste-water contain Cr(VI) and malachite green," *Applied Catalysis B: Environmental*, vol. 205, no. 5, pp. 9–15, 2017.

[35] Z. Cheng, W. Fang, T. Zhao et al., "Efficient visible-light-driven photocatalytic hydrogen evolution on phosphorus-doped covalent triazine-based frameworks," *ACS Applied Materials Interfaces*, vol. 10, no. 48, pp. 41415–41421, 2018.

[36] K. Wang, L.-m. Yang, X. Wang et al., "Covalent triazine frameworks via a low-temperature polycondensation approach," *Angewandte Chemie International Edition*, vol. 56, no. 45, pp. 14149–14153, 2017.

[37] D. Y. Osadchii, A. I. Olivos-Suarez, A. V. Bavykina, and J. Gascon, "Revisiting nitrogen species in covalent triazine frameworks," *Langmuir*, vol. 33, no. 50, pp. 14278–14285, 2017.

[38] J.-F. Moulder, W.-F. Stickle, P.-E. Sobol, and K.-D. Bomben, *Handbook of X-ray Photoelectron Spectroscopy*, J. Chastain, Ed., Perkin-Elmer Corporation, 1992.

[39] J. Zhang, J. Chen, Y. Wan et al., "Defect engineering in atomic-layered graphitic carbon nitride for greatly extended visible-light photocatalytic hydrogen evolution," *ACS Applied Materials & Interfaces*, vol. 12, no. 12, pp. 13805–13812, 2020.

[40] M. Liu, L. Guo, S. Jin, and B. Tan, "Covalent triazine frameworks: synthesis and applications," *Journal of Materials Chemistry A*, vol. 7, no. 10, pp. 5153–5172, 2019.

[41] Y. Zhang and S. Jin, "Recent advancements in the synthesis of covalent triazine frameworks for energy and environmental applications," *Polymers*, vol. 11, no. 1, p. 31, 2019.

[42] T. Feng, J.-M. Wang, S.-T. Gao et al., "Covalent triazine frameworks supported CoPd nanoparticles for boosting hydrogen generation from formic acid," *Applied Surface Science*, vol. 469, pp. 431–436, 2019.

[43] R. Kamai, K. Kamiya, K. Hashimoto, and S. Nakanishi, "Oxygen-tolerant electrodes with platinum-loaded covalent triazine frameworks for the hydrogen oxidation reaction," *Angewandte Chemie International Edition*, vol. 55, no. 42, pp. 13184–13188, 2016.